

# Modeling the Resolution for Photoacoustic Bio-Microscopy in the Giga-Hertz Frequency Range

Chukwunomso Agunwamba

Mathematics and Physics, Worcester Polytechnic Institute

NNIN REU Site: Center for Nanoscale Systems, Harvard University

NNIN REU Principal Investigator: Shriram Ramanathan, School of Engineering and Applied Sciences, Harvard University

Contact: nomnso@wpi.edu, shriram@seas.harvard.edu

## Abstract

Photoacoustic (PA) methods promise higher image resolution with an increase in the acoustic wave's frequency. However, they are effectively limited by the wave's penetration depth as the frequency enters the gigahertz range [1,2]. In this project, we explored the relationship between depth, initial center frequency, and amplitude for the acoustic pulse. First, arrangements of transducers and metallic particles were specified for the PA microscope. For the setup, a discrete time model was used to show how to obtain an image, to develop relations both for the resolution. This model was simulated in MATLAB®.

## Introduction

Previously, in a paper [3] by Daniel Wulin and Shriram Ramanathan, curves relating the center acoustic frequency for metallic and silica particles to their radii were generated and discussed. For a fluid, they also showed how the initial center frequency of a Gaussian acoustic pulse is downshifted as a function of depth traveled. This project proposes several transducer and metallic particle arrangements for a PA bio-microscope. It can be useful for non-invasive examination of the structure of biological media and molecules (such as fat) and individual cells or tissues. It uses acoustic waves generated from the elastic response of nano-sized metallic particles to a laser pulse train. The lateral and axial resolutions from the resulting image are modeled in terms of the maximum center frequency allowed by selected biological media and the acoustic pulse's bandwidth.

## Theory

The acoustic pulse,  $h(m)$ , would pass through a sequence of interfaces while experiencing reflections represented as  $r_k$ , transmission represented as  $(1-r_k)$ , and attenuation between interfaces represented as  $\alpha(\omega l)$ . The absorption coefficient is a function of the center frequency. Its expression depends on the medium. In the MHz range, this curve has been determined for several biological media. For example, attenuation coefficient for water is known to have an  $f^2$  relationship with frequency in the MHz range [4]. It is assumed that the signal containing reflected-acoustic pulses and the signal containing emitted-acoustic pulses are spatially and temporally sampled once they are received.

The signal coming from the imaged sample is a superposition of scaled and delayed pulses that have the same profile as the original emitted pulse. It is assumed that there is weak temporal dispersion of the composite acoustic pulse formed by the superposition of several center frequencies,  $\omega_j$ . The de-convolved spectrum is, therefore, a linear combination of scaled and delayed sinusoidal functions in the frequency domain.  $S(\omega)$  is

the impulse response of the transducer, while  $H(\omega, \omega_j)$  is the spectrum of Gaussian acoustic pulse with a center frequency of  $\omega_j$ . The spectrum,  $X(\omega, \omega_j)$ , contains the information about attenuation, reflection, and the time delay for each echo pulse in the signal.

The axial resolution [5,6] is treated as being quite independent of the center frequency. The stress and thermal confinements of the laser pulse temporal width is given by  $t_s$  and  $t_{th}$  [7]. This, in turn, limits the temporal width of the acoustic pulse it modulates.  $V_o$  is the velocity of the acoustic pulse in the medium housing the metallic particles and the transducers.  $V_j$  is in the space after the  $j$ th interface. To calculate depth, the velocity of the acoustic pulse is assumed constant within the imaged medium, only depending on the center frequency. It is also assumed that the medium housing the metallic particles and the transducers has an impedance matching the imaged sample.

The lateral resolution is obtained using the diameter of the transducer,  $d_j$ , its focal length, the maximum center frequency,  $\omega_{l,att}$ . The frequency,  $\omega_{l,att}$ , is the highest frequency with the minimum detectable intensity in the signal.

$$Y(\omega) = S(\omega) \sum_j N(\omega, \omega_j) H(\omega, \omega_j), \quad X(\omega) = \sum_{k=1}^J C_k(\omega_j) e^{-\alpha(k, \omega_j) \omega l}$$

$$H(\omega, \omega_j) = \left( \frac{I_0}{\sigma_l \sqrt{2\pi}} \right) \left[ e^{-\frac{(\omega - \omega_j)^2}{2\sigma_l^2}} \right]$$

$$C_k^2(\omega_j) = C_{k-1}^2(\omega_j) e^{-\left( \alpha(\omega_j) \right) \Delta t_k(\omega_j)} \left[ (1 - r_{k-1})^2 \right] (r_k) / (r_{k-1})$$

Here,  $\omega = 2\pi \frac{k}{T_s}$ ,  $k$  is frequency in Hz, and  $F_s$  is the sampling frequency in Hz satisfying the Nyquist rate.

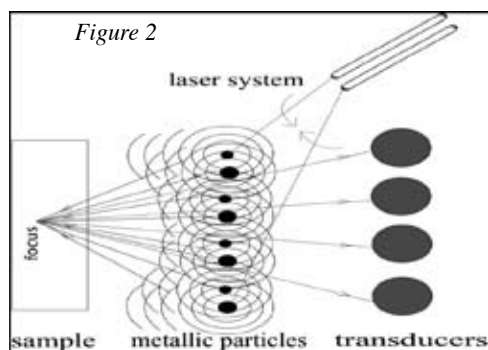
$$\text{Single Transducer Axial resolution} = R_A = \frac{V_o}{2 \times \text{FWHM} \left( \left| S(\omega) \sum_j H(\omega, \omega_j) X(\omega, \omega_j) \right| \right)} \approx t_a \times \min(V_j)^{1/2}$$

Here, the initial acoustic pulse temporal width =  $t_a \approx \min(t_s, t_{th})$

Highest center frequency detected at the transducer after being attenuated by the medium =  $\omega_{l,att}$

$$\text{Lateral resolution} = R_L = \frac{\lambda_o \times \text{focal length}}{d_l} = \frac{2\pi V_o \times \text{focal length}}{\omega_{l,att} \times d_l}$$

The depth profile is resolved with time, under the assumption of a linear relationship between reflection depth and ‘time-of-flight’. Here, the time-of-flight is the time for the wave to travel from the metallic particle(s) to an interface in the sample and to a receiving transducer. The assumption of a linear relationship implies that the wave maintains a constant velocity within each sub-medium of fixed characteristic impedance. The velocity only changes to a new value when the wave enters a region having a different characteristic impedance.



## Design

In Figure 2, a single laser beam excited a metallic particle or a cluster of metallic particles. (The black and the blue arrows trace the path of the rays to the transducer.) To direct and focus the beam, the light, from two lasers, swept in the directions indicated by the green arrows. The sweeping can also be done by one laser and a beam splitter. The sweeping action caused a relative time delay and a sequential excitation of the metallic particles. A curved wave front was created, according to Huygens’s principle. This idea was adapted from a description in a paper by P. N. T. Wells [8]. There, he describes how the sequential excitation of elements in a transducer array focuses and directs the acoustic wave beam. The difference is that a laser system and metallic particles are used in generating the acoustic wave in this paper.

The pulse-echo method relied on waves that are reflected at interfaces with mismatched acoustic impedances (See Figures 3 and 4). At any such interface, a fraction of the wave was transmitted into the new medium while the other portion was reflected. Each transducer element recorded the amplitude of the acoustic wave that passed by its position.

## Conclusion

A discrete pulse-echo model was developed and simulated in MATLAB to explore how the combination of high acoustic frequency, with the transducer setup, density of metallic particles, and choice of center frequencies, can make possible very fine resolutions in the range between micrometer and nanometer scales. Some follow up studies include: modeling how the nanoparticles control and shape the wave fronts in time and space, studying different materials and fluids for housing the nano-particles and the transducer, and making measurements of the attenuation coefficient of biological media in the giga-hertz range.

## Acknowledgments

The author acknowledges funding from the NNIN Research Experience for Undergraduates Program through Harvard University for this part of the research.

## References

- [1] “Photoacoustic imaging in biomedicine” by M. Xu, and L.V. Wang, Rev. Sci. Instrum. 77, 041101 (2006).
- [2] “Acoustic Microscopy: Biomedical Applications” by Ross A. Lemons, and Calvin F. Quate, Science, New Series, Vol. 188, No. 4191. (May 30, 1975), pp. 905-911.
- [3] “Non-invasive high-resolution acoustic microscopy technique using embedded nanostructures” by Daniel Wulin, and Shriram Ramanathan, Mater. Res. Soc. Symp. Proc. (2007).
- [4] “Ultrasonic imaging of the human body” by P N T Wells, Rep. Prog. Phys. 62 (1999) 671-722.
- [5] “Advances In Ultrasound Biomicroscopy” by F. Stuart Foster, Charles J. Pavlin, Kasia A. Harasiewicz, Donald A. Christopher, and Daniel H. Turnbull, Ultrasound in Med. & Biol., Vol. 26, No. 1, pp. 1-27, 2000.
- [6] “Analytic explanation of spatial resolution related to bandwidth and detector aperture size in thermoacoustic or photoacoustic reconstruction” by Minghua Xu and Lihong V. Wang, Phys. Rev. E 67, 056605 (2003).
- [7] “Photoacoustic imaging in biomedicine” by M. Xu, and L.V. Wang, Rev. Sci. Instrum. 77, 041101 (2006).
- [8] “Ultrasonic imaging of the human body” by P N T Wells, Rep. Prog. Phys. 62 (1999) 671-722.

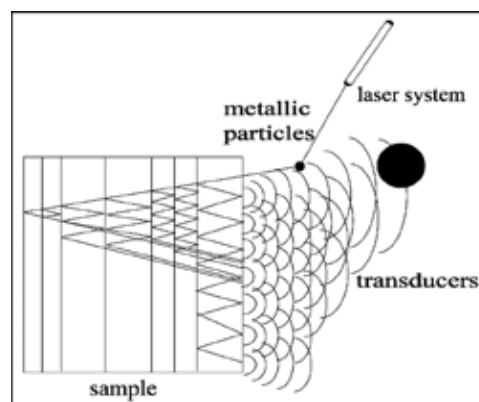


Figure 3: Reflections, transmissions, and absorptions occur each time a ray path meets an interface.

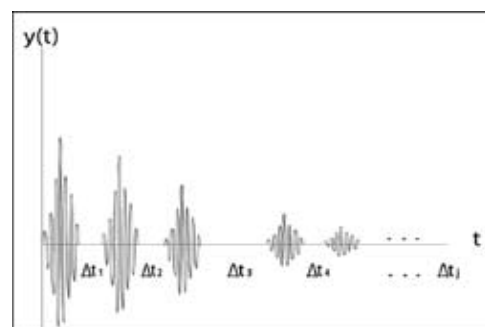


Figure 4: The echo signal as a combination of delayed pulses. The delay depends on the acoustic wave velocity in the sample and the distance between interfaces. These dependencies could cause the echoes to overlap.

# Electrical Charge on a Nanofiltration Membrane

**Kasiem Anderson**

**Biomedical Engineering, Georgia Institute of Technology**

*NNIN REU Site: Howard Nanoscale Science and Engineering Facility, Howard University*

*NNIN REU Principal Investigator: Dr. Kimberly Jones, Civil Engineering, Howard University*

*NNIN REU Mentor: Dr. Jermev Matthews, Civil Engineering, Howard University*

*Contact: gth707m@mail.gatech.edu, kljones@howard.edu, jermevm@gmail.com*

## Abstract

Nanotechnology applications have become useful in the optimization of filtration membranes. The extended Nernst-Planck (ENP) equation is a complex mathematical model that can be manipulated to calculate and predict flux, rejection, or electric charge across a membrane. Using the MATLAB® software, a program can be created to calculate these theoretical values that will guide the fabrication of membranes with optimized performance as well as shed light on the understanding of experimental data. With this knowledge, progression with nanofiltration membranes will be quickened, and we can sooner be able to use them for more practical applications of filtering water such as the purification and reuse of drinking water.

## Introduction

The ENP equation is a complex equation using the ionic diffusion, electric field gradient, and convection of a membrane to solve flux, or the ability of a particular species to pass through the membrane, such that flux is equal to the convection minus the diffusion and electric field gradient. As such, the equation does not have any relation to the mechanistic structure of the membrane, but rather the performance of the membrane.

As a complex differential equation needing the Runge-Kutta method to be solved, manipulation of the ENP equation can be quite time consuming and difficult. Therefore, it is quite appropriate to create a program that will solve for the various variables needed to progress in nanofiltration membrane optimization.

The Runge-Kutta is a method of integration that involves a recursive method of averaging the derivative at several points, then adding this new number to a sum variable until the last point of integration is reached. There are multiple versions of the Runge Kutta with varying levels of accuracy. This alone may require many iterations, so using a computer will not only save time, but allow for a more accurate version of the Runge Kutta, and likewise attain a most accurate result.

## Using the Model to Write Program

Using the MATLAB software, it is essential to write the ENP equation and its associated equations into the .m file. The ENP equation solutions must fall under the restrictions stated by the electro-neutrality condition and the under zero current condition. Using the Runge-Kutta method of solving the system of differential equation for the potential and concentration

gradients, we are able to move between the flux, the electric potential across the membrane, as well as solve for the rejection of ions within a few more steps.

## Future Progress

We were not able to complete the program using the ENP equation but have made some progress with it. As such, the first step is to continue the work we have done, and find a way to complete an efficient and accurate method of programming the ENP equation into MATLAB, or some other programming software application.

A logical next step to take is to continue working with the extended Nernst Planck equation to allow one to solve for any of the many variables of the model. Practically speaking, what is necessary is to find out how to reach the desired settings of the nanofiltration membrane, especially the charge across the membrane. Eventually, with work, nanofiltration will be used more and more for drinking water filtration, to medical uses throughout the world. Naturally this will be expedited by the use of computers wherever possible, such as the math calculations assigned.

## Acknowledgements

National Nanotechnology Infrastructure Network Research Experience for Undergraduates Program; Howard Nanoscale Science and Engineering Facility; Dr. Kimberly Jones; Dr. Jermev Matthews; Dr. Gary Harris; Mr. James Griffin; Mr. Aaron Jackson.



# Electron Transport in Silver Silicon Composite Film

Ian Broderick

Physics, Carleton College

*NNIN REU Site: Howard Nanoscale Science and Engineering Facility, Howard University*

*NNIN REU Principal Investigator: Dr. Clayton Bates, Electrical Engineering, Howard University*

*NNIN REU Mentor: Dr. Chichang Zhang, Electrical Engineering, Howard University*

*Contact: broderii@carleton.edu, bates@msrce.howard.edu*

## Abstract

Composite films of silver (Ag) nanoparticles embedded in an n-doped silicon (Si) matrix exhibit strong photo responses when exposed to infrared spectrum, especially in the 1-15  $\mu\text{m}$  wavelength range. The focus of this project is to quantify the Hall effect on a 3  $\mu\text{m}$  thick composite film composed of 18% Ag grown on a highly resistive Si substrate. The measured Hall current is related to the electron mobility and reflects the responsivity of the future infrared detector. Samples were created via magnetron co-sputtering at 550°C using Argon plasma at 3.5 mTorr. Four ohmic contacts of chromium (Cr) and gold (Au) were evaporated on the sample, using e-beam and thermal deposition followed by rapid thermal annealing, to employ the Van Der Pauw method of Hall measurement. Hall measurements were taken at the National Institute of Standards and Technology between 77 K and 300 K.

## Introduction

Silver nanoparticles display strong photo responses to infrared spectrum. To create a device that takes advantage of this characteristic, Ag will be co-sputtered with highly n-doped Si to form a matrix with embedded Ag nanoparticles. In order to fabricate this device, we must characterize its responsivity, electron mobility and potential lifetime. Fortunately all this can be extracted from measurements of the Hall currents, which is a direct measurement of the mobility and rapidity of the electrons in the material. Essential to the film are isolated small non-chemically bonded Ag nanoparticles; isolated to avoid shorts, small to increase the surface area and response strength, and non-chemically bonded to avoid unwanted silicides. To avoid the silicides, we made depositions at 550°C which is low enough to prevent silicides and high enough that we get our silicon in crystal form. Taking into account the other specifications, this project aimed to accurately sputter a 3  $\mu\text{m}$  thick composite film of 18% Ag, 82% n-doped Si onto a Si substrate.

## Experimental Procedure

Our Ag and n-doped Si (resistivity: 1-5  $\Omega\text{cm}$ ) targets were placed in the Kurt J. Lesker CMS-18 Magnetron Plasma co-sputtering system. This system uses argon plasma and using different voltages can co-sputter two targets at varying rates. For both of our trials, 25A and 25B, the deposition temperature was 550°C and the Ar pressure was 3.5 mTorr. Both depositions ran for precisely 2.5 hours. Our first sample 25B had the following deposition specifics: base pressure of  $2.7 \times 10^{-7}$  Torr, Ag power supply of 12W ( $\sim 260\text{V}$  across target), Si power supply of 330 W ( $\sim 470\text{V}$ ). Our second sample, due to a realization that 25B had too much Ag, had a much lower Ag voltage: base pressure of  $5.0 \times 10^{-8}$  Torr, Ag power supply of 7W (152V), same

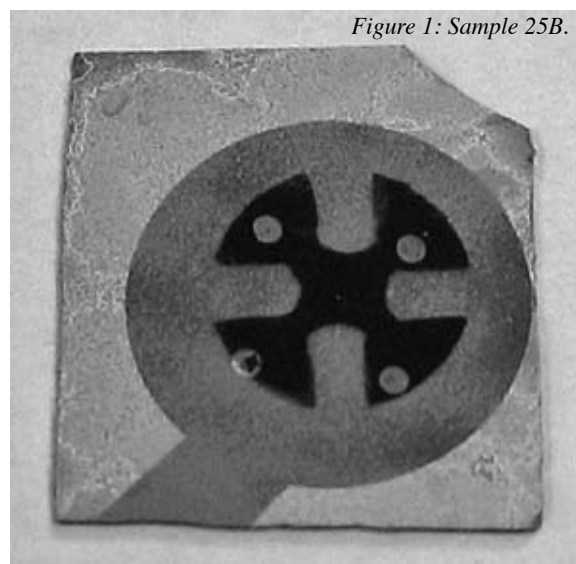


Figure 1: Sample 25B.

Si power supply. After deposition, four ohmic contacts had to be placed on the film for the future Hall measurements. To achieve this, we evaporated a 200Å layer of chromium followed by a 1500Å layer of gold, using e-beam and thermal evaporation respectively. The sample then underwent thermal annealing at 600°C for 30 seconds. The final product is shown in Figure 1.

At this point, we went to make the Hall measurements using the Van Der Pauw method. Detailed info on the exact specifics of this technique can be found at <http://www.eeel.nist.gov/812/hall.html>. The key variable defined by this experiment is  $\Sigma V_i$  which is the sum of all the positive magnetic field voltages minus the sum of all the negative field voltages (we used a magnetic field of 8000 Gauss). This value plugs into  $n_s = ((8 \times 10^{-8})IB)/(q \cdot \Sigma V_i)$  to get the number of mobile carriers. Finally this value, along with

the average resistivity,  $R_s$ , gives us the electron mobility of  $\mu = (R_s * qn_s)^{-1}$ . We took these mobility measurements at different temperatures from 77K to 290K to define the optimal operating temperature.

## Results and Discussion:

Figures 2 and 3 display the resistivity and electron mobility vs. temperature for both samples. As can be seen from Figure 3, the resistivity of sample 25B is far too low, implying too much silver. Later Rutherford back-scattering tests showed that indeed sample 25B was 22.5% Ag and that our corrective measures resulted in 11% Ag in 25A. Thus sample 25B was relatively useless for this project.

25A was more hopeful, in that it displayed the expected mobility vs. temperature relationship; initially a positive relationship due to decreased impurity scattering, later to taken over by a negative relationship caused by lattice vibrations. The final issue we took with sample 25A was how low the Hall mobility was, which should have been in the  $10^3$ ,  $10^4$  range. This could probably be solved by using a more highly doped Si target (of resistivity around 0.001-0.006  $\Omega\text{cm}$ ) which was our original intent (but the target cracked). Also more accurately attaining 18% Ag would help in this matter.

## Future Work

For the future creation of an infrared detector, more characterization is required. Specifically, the measurement of the responsivity of the device to different incident wavelengths at varying operating voltages. After that, this project only needs optimization of the fabrication process and creating the final product.

## Acknowledgements

I would like to thank Dr. Clayton Bates and my mentor Dr. Chichang Zhang for guidance and assistance during my research. I would also like to thank the National Nanotechnology Infrastructure Network Research Experience for Undergraduates Program and the National Science Foundation for funding. Finally I want to acknowledge Robert Thurber from the National Institute of Standards and Technology for providing the Hall measurement equipment.

## References

- [1] Shur, Michael. Physics of Semiconductor Devices. Prentice Hall. NJ, 1990.
- [2] Sze, Simon. Physics of Semiconductor Devices. Wiley-Interscience. 1981.
- [3] Zeghbroeck, Bart Van. "Principles of Semiconductor Devices" <http://ece-www.colorado.edu/~bart/book/> 2004.

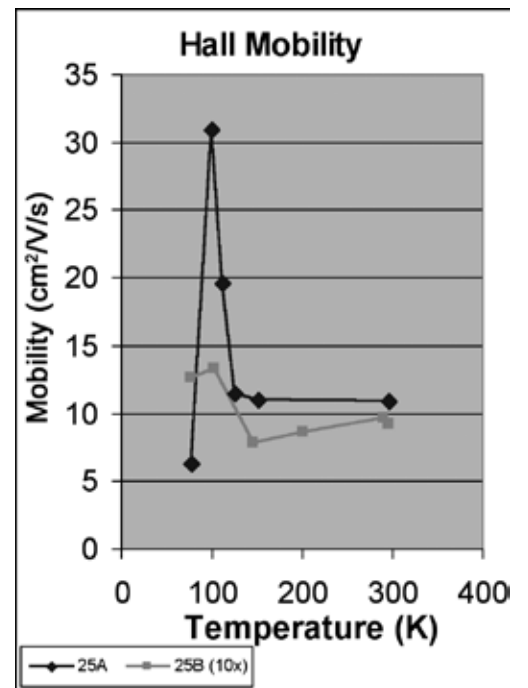


Figure 2: 25A, 25B Hall mobility.

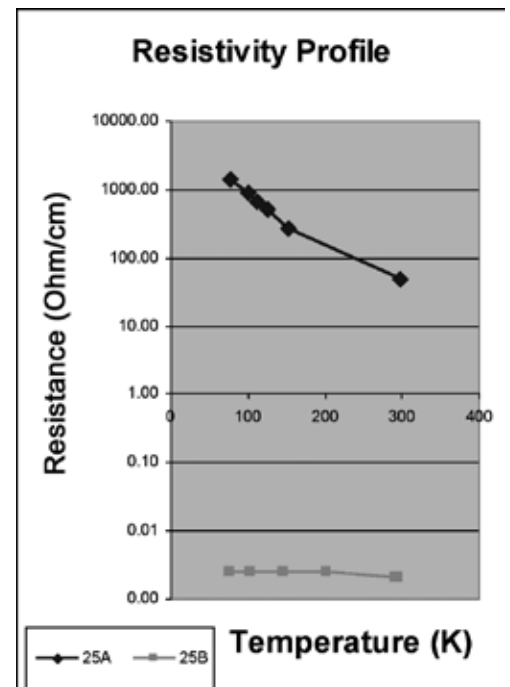


Figure 3: 25A, 25B Resistivity profiles.

# Simulation of Room-Temperature Terahertz Quantum Cascade Lasers with Varying Degrees of Transverse Confinement

**Nikhil Chandra**

Applied and Engineering Physics, Cornell University

*NNIN REU Site: Microelectronics Research Center, The University of Texas at Austin*

*NNIN REU Principal Investigator: Dr. Matthew Gilbert, Microelectronics Research Center, The University of Texas at Austin*

*NNIN REU Mentor: Dr. Leonard F. Register, Electrical and Computer Engineering, The University of Texas at Austin*

*Contact: nsc22@cornell.edu, mgilbert@mail.utexas.edu, register@mer.utexas.edu*

## Abstract

The transport and scattering of electrons through quantum wire aluminium gallium arsenide (AlGaAs)/GaAs heterostructures were simulated for various diameters. The effects of transverse confinement on non-radiative electron transitions were studied in an attempt to improve lasing efficiency at room-temperature.

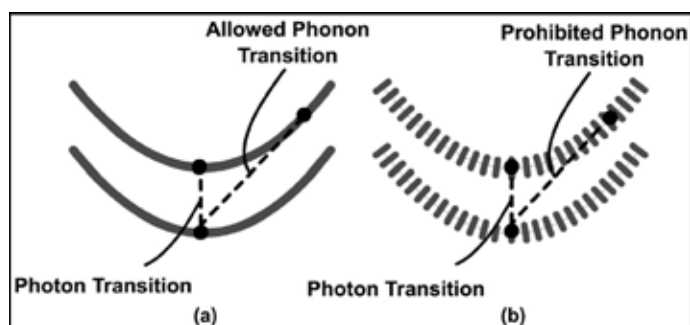


Figure 1: Energy bands; (a) without transverse confinement, and (b) with transverse confinement.

## Introduction

Quantum cascade lasers (QCLs) emit radiation when electrons passing through a layered heterostructure undergo transitions between energy eigenstates and then emit photons. Currently, terahertz QCLs only operate at very low temperatures, as electrons absorb thermal energy and rise in energy bands associated with dimensions transverse to the direction of transport, undergoing transitions to lower eigenstates by emitting LO-phonons instead of photons (Figure 1a). LO-phonons are bosons that correspond to high-frequency longitudinal lattice vibrations. Applications of terahertz QCLs would be significantly economized by successfully achieving room-temperature operation. Theoretically, transverse confinement of the superlattice in quantum wires would discretize energy bands associated with dimensions transverse to the transport direction. This would obstruct the absorption of thermal energy by electrons, and subsequent transitions between eigenstates would result in the radiative emission of photons instead of the non-radiative emission of phonons (Figure 1b).

The focus of this project lay in qualitatively determining the efficacy of transverse confinement in improving the radiative efficiency of a terahertz QCL operating at room-temperature. We designed a heterostructure that possessed desirable spacings and resonances between energy eigenstates. This was followed by the simulation of the transport and scattering of electrons through quantum wires of various diameters with this heterostructure, using a quasi-three-dimensional non-equilibrium Green's function (NEGF) simulator entitled "Schrödinger Equation Monte Carlo 3D" (SEMC3D). Only scattering by phonon emission was considered. Reductions in non-radiative phonon transition rates were associated with increased radiative photon transition rates, and vice versa. Transitions triggered by phonon absorption were ignored.

## Method

We found the energy eigenstates of a potential profile using a shooting-point eigenvalue solver. The profile consisted of wells and barriers that corresponded to the GaAs/AlGaAs heterostructure of a single QCL module, over which a potential drop of 46 meV was applied. The widths of the wells and barriers were adjusted and the effective mass of each region was tuned until desirable spacings and resonances between energy eigenstates were obtained.

Figure 2 displays the final heterostructure designed, along with the energy eigenstates superposed with their probability densities.  $E_5$ 's wavefunction was concentrated in the first two wells to ensure that electrons injected into this level would fall to  $E_4$  or  $E_3$  within these wells, preferably by emitting a photon. Population inversion was promoted by evenly spreading out the probability densities of  $E_4$  and  $E_3$  between all three wells to provide rapid tunneling, and by setting the energy gap between

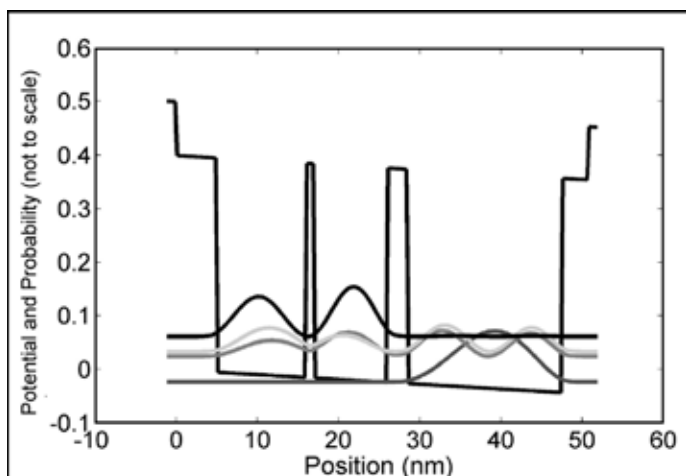


Figure 2: Potential profile with energy eigenstates and probability densities.

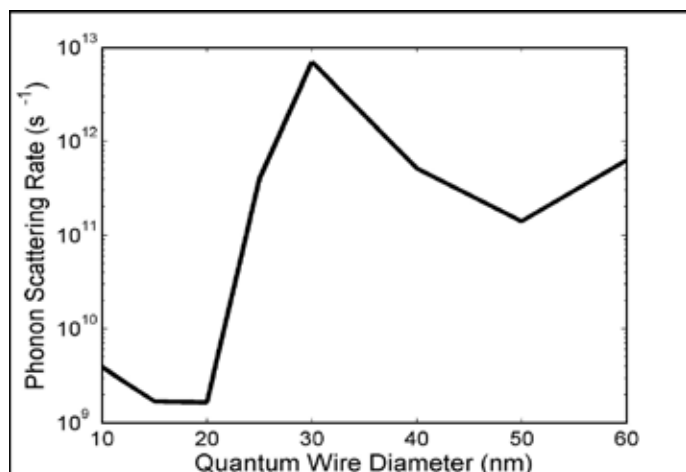


Figure 3: Variation of non-radiative phonon scattering rate with diameter.

$E_3$  and  $E_2$  to roughly equal the LO-phonon energy of GaAs, as this would encourage rapid transitions between these levels by phonon scattering.

We built three-dimensional potential fields corresponding to quantum wires of different diameters using this heterostructure, to be loaded into SEMC3D. However, since the heterostructure would no longer be isolated from the “outside world,” a slight offset in the spacings between the energy eigenstates as calculated by SEMC3D was expected. To discover the true spacings between the eigenstates, we configured SEMC3D to inject electrons into the profile over a range of energies, and calculated the transmission probability (i.e., the likelihood that an injected electron would traverse the entire length of the module). Energies for which there was a spike in the transmission probability corresponded to the now quasi-bound eigenstates.

To ensure the qualitative accuracy of the simulation, we varied the LO-phonon energy until the electron scattering rate by the emission of phonons in the third well was maximized. This was vital to ensure rapid depopulation of  $E_4$  and  $E_3$ , promoting population inversion. The LO-phonon energy settled upon was 36.263 meV. For each quantum wire diameter, we used SEMC3D to calculate the energies and wavefunctions of the two-dimensional transverse energy subbands. We followed this by injecting electrons into  $E_5$  for each of these subbands. In each case, the average phonon scattering rate in the first two wells was calculated using the average self energy. A Fermi-weighted average of the subbands’ scattering rates was used at 300 K to understand the effects of transverse confinement on scattering by phonon emission at room-temperature. We performed this procedure for quantum wires with diameters of 10 nm, 15 nm, 20 nm, 25 nm, 30 nm, 40 nm, 50 nm and 60 nm.

## Results

The phonon scattering rate decreased precipitously for wires with diameters below 30 nm (Figure 3). The peak in scattering rate observed for 30 nm was attributed to resonances between the transverse subbands. The lowest scattering rate was achieved at a diameter of 20 nm. Further reduction in diameter led to an increase in the scattering rate. This was attributed to an increase in the overlap between the initial and final carrier states between the ground states of  $E_5$ , and  $E_3$  and  $E_4$ .

## Conclusion

We have qualitatively demonstrated that the discretization of energy bands by transverse confinement decreases the likelihood of non-radiative scattering by phonon emission. New methods for the construction of quantum wire heterojunctions may provide a means to implement transverse confinement in terahertz QCLs, enabling room-temperature operation.

## Acknowledgements

I would like to thank Dr. M.J. Gilbert, Dr. L.F. Register, Dr. S. Banerjee, Ms. Jean Toll, the National Nanotechnology Infrastructure Network Research Experience for Undergraduates Program and the NSF.

## References

- [1] B.S. Williams, S. Kumar, and Q. Hu, Opt. Soc. of Amer. (2005).
- [2] R. Köhler, A. Tredicucci, F. Beltram, H.E. Beere, E.H. Linfield, A.G. Davies, D.A. Ritchie, R.C. Iotti, and F. Rossi, Nature 417, 156 (2002).
- [3] B.S. Williams, H. Callebaut, S. Kumar, Q. Hu, and J.L. Reno, Appl. Phys. Lett. 82, 1015 (2003).

# Enhanced Laser Cooling Using Ion-Doped Nanopowders: Engineering and Harvesting Atomic Vibrations

Philip Hebda

Mathematics and Physics, Purdue University

NNIN REU Site: Michigan Nanofabrication Facility, The University of Michigan Ann Arbor

NNIN REU Principal Investigator: Dr. Massoud Kaviany, Department of Mechanical Engineering, University of Michigan

NNIN REU Mentor: Jedo Kim, Department of Mechanical Engineering, University of Michigan

Contact: phebda@purdue.edu, kaviany@umich.edu, jedokim@umich.edu

## Abstract

This research focused on maximizing the overall cooling rate to cool solids from room temperature to the cryogenic temperature range by advancing the existing theoretical treatments. At the atomic level, laser cooling is described through the energy transfer mechanisms among photons, electrons, and phonons. The cooling rate is dependent on the interactions and properties of the host atoms, the optically-active dopant, and the coupling between these three carriers [1]. Investigated parameters included the electron-phonon coupling coefficient and the phonon density of states (DOS) using the Debye-Gaussian model, both of which affect the phonon-assisted photon absorption rate, the target phonon energy, and the nonradiative decay rate. To enhance the cooling rate, doped nanopowders are used over bulk since the DOS of nanopowders has broader peaks [2].

## Background

The ultimate goal in laser cooling research is to create a refrigeration unit capable of reaching the cryogenic temperature range. Since it lacks moving parts, such a device would have a longer lifetime than other coolers. The largest reported temperature drop has been 70 K from room temperature, and the process has been observed as low as 77 K [3].

## Laser Cooling Process

The solid to be cooled is composed of an ionic host doped with an optically-active rare-earth ion. Incident photons have a frequency tuned slightly lower than the resonance transition of the dopant. In order for an electron of the dopant to absorb an incident photon, a phonon from the host must also be absorbed so that the sum of the photon and phonon energies equals the resonance transition. The electron then decays back to the ground state either radiatively, with the emission of a photon, or nonradiatively, with the emission of phonon(s) and a photon. Cooling occurs if the average emitted photon has a greater energy than the incident photon.

## Cooling Rate Equation

In Figure 1, the cooling rate equation is given in the unit of watt [1]. The variables which vary with the selection of host include

$$\dot{S}_{ph-e-p} = \frac{\pi \hbar}{2 \epsilon_0 m_{eff}} (s_a \cdot \hat{i}_e)^2 \varphi_{e-p,0}^2 \frac{D_p(E_p) f_p^o(E_p) \hbar \omega_{ph,i} n_d L}{E_p^3 u_{ph}} Q_{ph,i} \left(1 - \frac{\lambda_{ph,i}}{\lambda_{ph,e}} \eta_{e-ph}\right)$$

Figure 1: Cooling rate equation.

the effective mass of the constituent atoms  $m_{eff}$ , the electron-phonon coupling coefficient  $\varphi'_{e-p,0}$ , the phonon DOS  $D_p$ , the target phonon energy  $E_p$ , the Bose-Einstein distribution  $f_p^o$ , and the internal quantum efficiency  $\eta_{e-ph}$ . Other factors from the equation, which vary with the properties of the optically-active dopant, laser irradiation, and the structure of the sample, include the photon-electron coupling coefficient  $s_a \cdot \mu_e$ , the frequency  $\omega_{ph,i}$  and wavelength  $\lambda_{ph,i}$  of the laser photons, the number density of the dopant  $n_d$ , the length of the solid  $L$ , the speed of light  $u_{ph}$ , the incident laser power  $Q_{ph,i}$ , and the average wavelength of the emitted photons  $\lambda_{ph,e}$ .

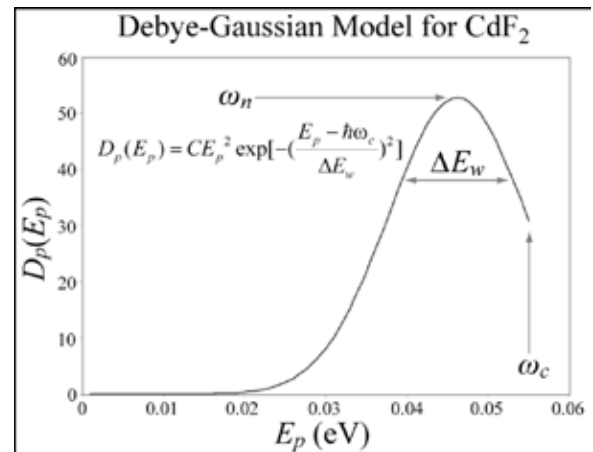


Figure 2: DOS for  $\text{CdF}_2$  using the Debye-Gaussian model, shown with the DOS equation, where the constant  $C$  is dependent on the cut-off frequency  $\omega_c$  ( $C = 26587.7 \text{ eV}^3$  for  $\text{CdF}_2$ ).

## Phonon DOS

The density of states (DOS), which gives the number of phonon modes for a given energy, was estimated using the Debye-Gaussian model (Figure 2). The peak value was calculated from the natural frequency  $\omega_n$ , the cut-off frequency  $\omega_c$ , and the width of the peak  $\Delta E_w$ . The area under the curve was normalized to one, so a lower cut-off frequency increased the peak value.

By using the harmonic oscillator model, cut-off frequencies were calculated for various fluorides, chlorides, and oxides from the spring force constant and effective mass between the anion-cation pair. In addition to increasing the peak DOS value, lower cutoffs augment the cooling rate by increasing the internal quantum efficiency and decreasing the target phonon energy. From the calculations, chloride paired with a heavy cation would maximize the cooling rate through these factors.

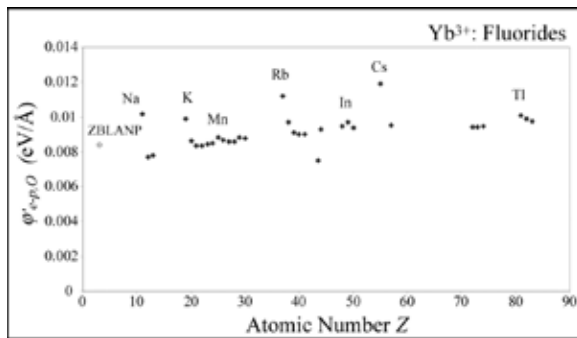


Figure 3: Electron-phonon coupling coefficient for various cations in fluoride glass.

## Electron-Phonon Coupling

In the harmonic oscillator model, the dopant absorbs phonons from the vibrations of a neighboring anion. When an anion-cation pair oscillates with respect to the dopant, the anion-dopant bond length changes, changing the potential of the dopant's valence electrons. As the coupling factor is increased through host selection, the same anion-dopant contraction or dilation increases the potential change of the electrons. The electron-phonon coupling coefficient was calculated for Yb<sup>3+</sup>-doped fluorides (Figure 3). Electron-phonon coupling increases slowly with atomic number and peaks at the alkali metals. Rubidium and cesium fluorides are the optimal cations for maximizing electron-phonon coupling.

## Nanopowders

The properties of nanopowders have been found to enhance the cooling rate over bulk materials by increasing the number of energy carriers in laser cooling, specifically phonons and photons [2]. Calculations show that the DOS of nanopowders is on average larger at the relevant phonon energies. Photon

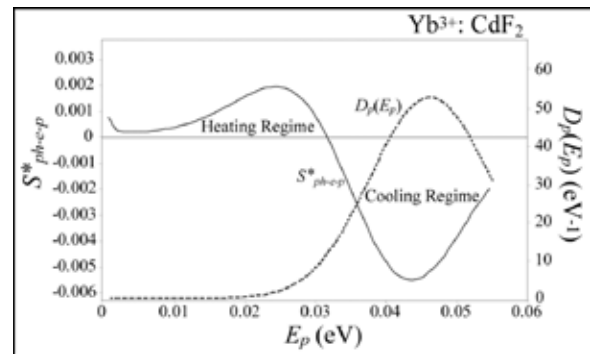


Figure 4: Calculated cooling rate (normalized per unit of input power  $Q_{ph,i}$ ) and normalized DOS vs. target phonon energy.

scattering in random nanopowders leads to photon localization, where photons do not propagate through the solid but are spatially restricted to a region. This leads to a much higher photon density per input power.

## Conclusions

The selection of an ionic host material has been discussed through the DOS and the electron-phonon coupling coefficient. From the results, ideal cations are rubidium and cesium. Currently, fluoride is used as the anion because it is known to be optically transparent to the laser photons; more research is needed for other anions.

In Figure 4, the normalized cooling rate varies with the target phonon energy. In the heating regime, the target phonon energy is too low, so each instance of radiative decay does not remove a sufficient amount of phonon energy to overcome the heating of nonradiative decay. The target phonon energy which provides the maximum cooling rate (most negative) is shifted slightly to the left of the DOS peak value due to the Bose-Einstein distribution and the  $E_p^3$  term in the denominator of the cooling rate equation.

## Acknowledgements

I would like to thank Dr. Massoud Kaviany for allowing me to work in the Heat Transfer Physics Laboratory and Jedo Kim for mentoring me on my project. This project was supported by the National Nanotechnology Infrastructure Network Research Experience for Undergraduates Program and the National Science Foundation.

## References

- [1] Kim, J. and M. Kaviany, "Material Selection Optimization for Ion-Doped Laser Cooled Diatomic Crystals," (unpublished).
- [2] Ruan, X. L., and M. Kaviany, Phys. Rev. B 73, 155422 (2006).
- [3] Ruan, X. L., and M. Kaviany, J. Heat Transfer 129, 3 (2007).



## What Makes Peacock Feathers Colorful?

Suntrana (Tran) Smyth

Physics, University of Alaska, Fairbanks

NNIN REU Site: Cornell NanoScale Science & Technology Facility, Cornell University

NNIN REU Principal Investigator: Professor Sandip Tiwari, Electrical and Computer Engineering, Cornell University

NNIN REU Mentor: Brian Bryce, Electrical and Computer Engineering, Cornell University

Contact: suntranafs@hotmail.com, st222@cornell.edu, babryce@gmail.com

### Introduction

The iridescence of peacock feathers is fascinating because of their range of colors and their brightness in a filament. Color can arise from wavelength selective absorption and wavelength selective reflection. Bright colors of many butterflies are now known to arise from reflection. Yoshioka and Kinoshita [1] found that the pigmentation in peacock feathers, instead of reflecting light, serves "...to absorb the randomly scattered light and [thus] make vivid the interference color." Zi et al. concluded that periodic structures caused the reflection properties that lead to the colors [2]. We undertook this effort to clarify the nature of the color phenomena in peacocks in view of earlier seemingly contradictory reports.

### Previous Work

Zi et al. [2] of Fudan University reported that two mechanisms are the cause of the iridescent colors in peacock feather barbules: varying size of the lattice constant and varying numbers of melanin rod layers normal to the cortex surfaces. Zi found that the green and blue barbule lattice constants were  $\sim 150$  nm and  $\sim 140$  nm respectively. The authors concluded that that Fabry-Perot interference was central to the coloration phenomena; the number of melanin rod layers parallel to the cortex surface was reported as " $\sim 9$ -12 for the blue and green barbules, and  $\sim 4$  for the brown barbules." Zi et al. also reported that the brown barbules possess a (non-square) rectangular lattice structure. They observed  $\sim 185$  nm along the direction perpendicular to the cortex surface by  $\sim 150$  nm along the parallel, and that brown barbule structures possess no air hole array between the melanin layers nearest to the surface [3].

### Methods and Observations

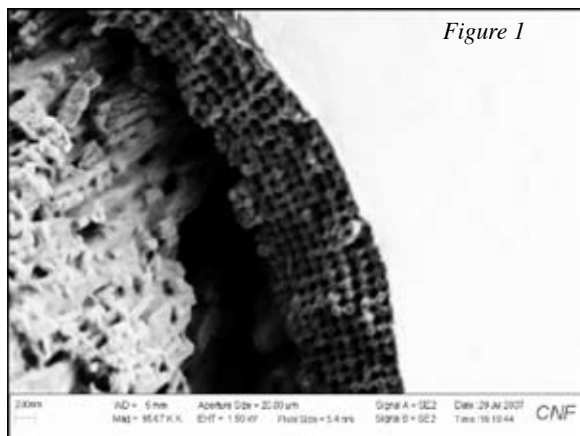
A peacock feather consists of a shaft from which barbs extend spirally. Tiny barbules protrude from each barb shaft. Visible under a scanning electron microscope (SEM), the perimeter of the cross-section of every barbule contains an ordered structure

(Figure 1). This structure consists of melanin rods interspaced with air holes, possibly integrated with keratin. We probed the structures by taking SEM images of feather cross-sections, measuring the geometries, and modeling the interaction of light striking those geometries with the M.I.T. electromagnetic equation program (MEEP).

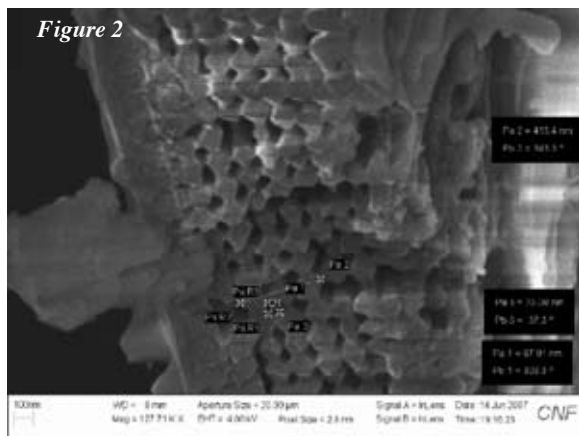
A spatially periodic dielectric material (in the case of peacock feather, melanin rods interspaced with air holes and keratin) that inhibits the propagation of light waves at certain frequencies and energies is called a "photonic crystal." It creates blocking and passing bands for photons similar to those of electrons in a semi conducting crystal. The feather structures give rise to what's known as a "partial" band gap, in which light is blocked (and therefore reflected) only at certain polarizations and angles of incident.

A variety of sampling techniques were attempted intending to produce high quality SEM images: barbule slices were imbedded in polymer which was cut to expose cross sections; glass and diamond microtomes were used to slice microscopic samples; an ineffectual attempt was made to break barbules cleanly using a hardened structure by cooling it with liquid nitrogen.

The most effective sampling strategy consisted of simply laying a barb down on copper tape, slicing the barbules from it with a razor blade, removing the stem, and gold sputtering to reduce charging by incident electrons. This yielded good quality SEM images of the barbule cross sections and of their longitudinal structure. However, there remained difficulties in structural measurement. First, even with sputtering, prolonged charging due to the electron beam was still apt to destroy parts of the sample. Second, the sputtering itself caused error, as it obscured the actual structures. Third, it was difficult to make a precise judgment as to the angles of the lense versus the cross-sectional face. Random errors were greatly reduced by averaging sizes of several lattices measured simultaneously.



With geometric data from these images, MEEP was used to simulate a Gaussian pulse of light with various frequencies and polarizations striking a square photonic crystal lattice of cylindrical void tubes of the observed diameters encased in melanin.



## Results

Our SEM images indicate that the blue and green barbu structures possess  $7.5 \pm 1$  melanin rod layers interspaced with air-holes parallel to the cortex surface. The brown barbu structures apparently possess  $7 \pm 1$  melanin rod layers interspaced with air-holes plus two outside layers of melanin without air-holes (Figure 2).

However, when the melanin rods were examined from a longitudinal view, large, previously unreported spherical distortions (Figure 3) were observed, indicating that the lattice structures are in fact three dimensional. In cross section, the green and blue barbu lattice structures appeared to be 2D and square, with lattice constants of  $154 \pm 10$  nm and  $156 \pm 10$  nm for the green and blue barbules respectively. We detected no difference in the perpendicular and parallel dimensions of the

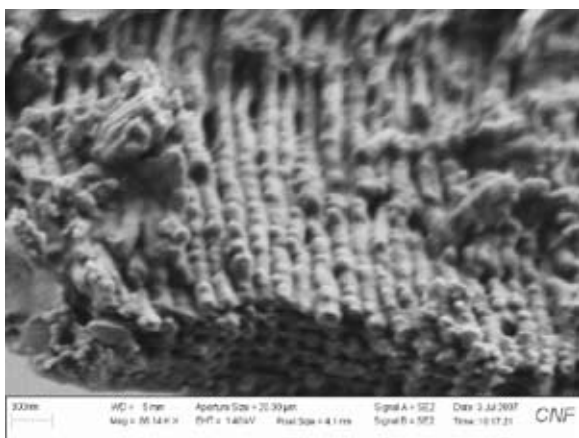


Figure 3: These bumps are of  $60\text{nm} \pm 20\text{nm}$  in radius.

lattice structure of the brown barbules, and observed a lattice constant of  $172 \pm 10$  nm.

Utilizing this data in our MEEP model produced a graph of light wavelength versus reflected power (Figure 4). There is correlation between the cylinder diameter to lattice constant ratio and wavelength of reflected light. Further work is needed in order to generalize these results for a complete model.

## Conclusions

We find, as did Li et al that the brown barbules, in contrast to blue and green, possess two melanin layers at the cortex lacking air spacing. Our data does not show a significant difference in number of total melanin layers parallel the cortex surface in differently colored barbules, differing with Zi et al.

Insofar as the structures are 2D, we find in contrast to Li et al, that the lattice structures of not only blue and green but also brown barbules are square. Our model does not show the cylindrical air hole radius to lattice spacing ratio affecting the range of the reflectance spectra as directly as theorized.

Over all, we find that a 2D model is insufficient to cause the broad range of light frequencies reflected from the different barbules and that 3D lattice, with spherical distortions along the melanin rods, are important to determining the color reflection properties of the peacock feather.

## Acknowledgements

The Intel Foundation; National Nanotechnology Infrastructure Network REU Program; National Science Foundation; Cornell NanoScale Facility; The Tiwari Group esp. Dr. Tiwari, and Brian Bryce; Cornell NanoScale Facility Staff; Cornell NanoScale Facility REU group.

## References

- [1] Yoshioka, S. and Kinoshita, S. 2002. Effect of Macroscopic Structure in Iridescent Color of Peacock Feathers. *Forma*, 17, 169-181.
- [2] Zi, J., Xindi, Y., Li, Y. et al. 2003. Coloration strategies in peacock feathers. *PNAS*. 100:12576-12578.
- [2] Li, Y. et al. 2005. Structural origin of the brown color of barbules in male peacock tail feathers. *Physical Review E* 72: 01902-1-01902-4.

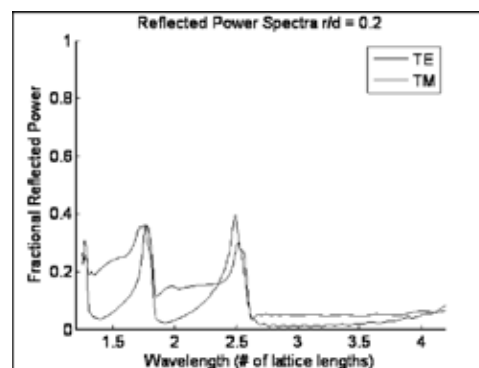


Figure 4: The right-most peak in the graph represents blue light.

# Thermal Transport in Silicon Nanowires

**Prem Vuppuluri**

Mechanical Engineering, University of Portland

*NNIN REU Site: Cornell NanoScale Science & Technology Facility, Cornell University*

*NNIN REU Principal Investigator and Mentor: Dr. Derek Stewart, Cornell NanoScale Facility, Cornell University*

*Contact: vuppulur08@up.edu, stewart@cnf.cornell.edu*

## Abstract

The thermal conductance of small diameter silicon (Si) nanowires was determined using a Density Functional approach. Nanowires were isolated from a bulk clathrate system with a unit cell of 30 Si atoms. The equilibrium coordinates of the atoms in the unit cell were determined through structural relaxation based on Hellmann-Feynman forces. Additionally, coordinate relaxations of a clathrate nanowire with terminating hydrogen atoms were also done. The force constant matrix was evaluated for a SiH nanowire with three unit cells. Phonon bands were obtained from the force constant matrix, and the transmission function was used to calculate thermal conductances for 20 temperature values. The high temperature conductance limit was  $4.75 \times 10^{-10}$  W/K.

## Introduction

Heat dissipation is a critical variable in the design and analysis of electronic systems. As device sizes approach the nanoscale order, constructing effective, thermally conductive fins becomes increasingly difficult. Transport of phonons and heat is ballistic in thermal conduits with length scales on the order of a nanometer. As a result, the analysis of the thermal conductance of nanowires requires a different approach from macroscopic systems. In this research, the thermal conductance was calculated by predicting how phonons would transmit through the system.

Phonons are the primary carriers of thermal energy in semiconductors. Phonons are waves created by the vibration of atoms in crystalline structures. The propagation of phonons through a lattice is responsible for thermal transport. In order to quantify the propagation of the phonons through the system, the force constant matrix of the nanowire system has to be determined. The phonon band diagram can be produced from the force constant matrix, and using this information, the transmission function of the system can be calculated as a function of frequency.

The transmission function  $T(\omega)$  can then be used to calculate the thermal conductance,  $\sigma$ , with the following equation [1]:

$$\sigma = \frac{1}{k_B T^2} \int_0^\infty (\hbar\omega)^2 \frac{e^{\hbar\omega/k_B T}}{(1 + e^{\hbar\omega/k_B T})^2} T(\omega) d\omega / 2\pi$$

where  $T$  is the temperature,  $\omega$  is the phonon frequency,  $k_B$  is the Boltzmann constant, and  $\hbar$  is the reduced Planck constant.

## Coordinate Relaxation

The first step in calculating the thermal conductance was to determine the atomic coordinates of the silicon nanowire taken

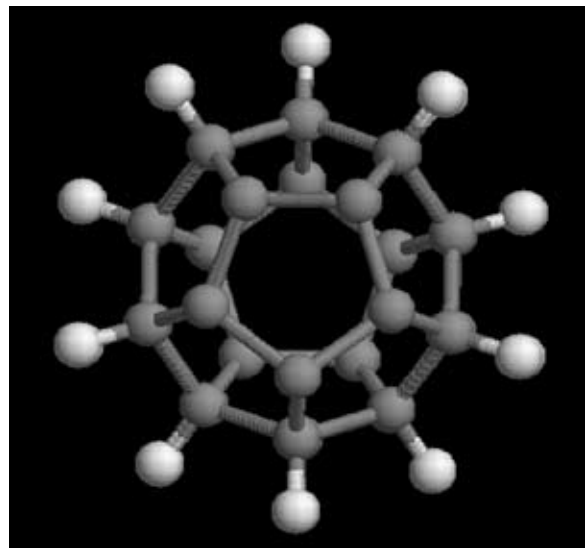


*Figure 1: Isolated clathrate silicon nanowire with terminating hydrogens. Diameter ( $d$ ) = 9.66 Å.*

directly from the bulk system. Figure 1 shows a top view of an isolated clathrate nanowire [2] with a unit cell composed of 30 Si atoms (dark grey) and 20 hydrogen (H) atoms (light grey).

Figure 1 was created using Si-Si bond lengths of 2.38 Å and Si-H bond lengths of 1.50 Å [3]. The structure contains only regular pentagons. Structural relaxations were done using SIESTA, a self consistent density functional code with a atomic orbital basis set [4]. For the relaxation analysis, a cutoff energy of 200 Ry and a double- $\zeta$  basis set were used. A force tolerance of 0.0025 eV/Å was taken for the calculation. Pseudopotentials were generated using Troullier and Martins' method [5]. 16 k-points in the  $z$  direction were used for the calculation.

The calculation of the relaxed coordinates produced a structure that looked very similar to the isolated structure shown in Figure 1. The relaxed nanowire had a diameter of 9.60 Å, as compared to the isolated nanowire which had a diameter of 9.66 Å. The lattice constant of the relaxed system was 10.31 Å, as opposed to a lattice constant of 10.59 Å.

### Force Constant Matrix Generation

A force constant matrix for the relaxed Si nanowire was generated by linking three unit cells together and disturbing atoms in the middle unit cell. The forces induced on neighboring atoms by the disturbance were used to generate the force constant matrix. The force constant matrix was used to create a phonon band diagram, and the transmission of phonons was calculated as a function of frequency. The phonon band diagram is shown in Figure 2, and the transmission function is shown in Figure 3.

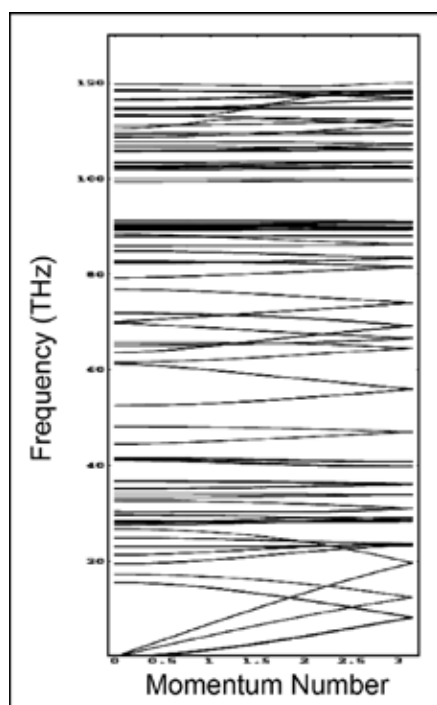
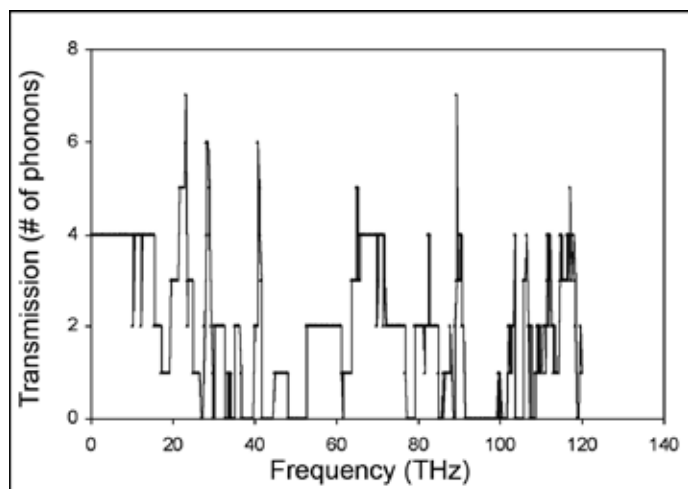


Figure 2, left:  
Phonon band diagram  
for terminated  
clathrate system.

Figure 3, below:  
Transmission function  
for terminated  
clathrate system.



The transmission function was generated from the phonon band diagram by observing the density of phonon bands at each frequency. The transmission function has sharp peaks at frequencies where the bands are flat and dense, and is zero for frequency ranges with no bands.

### Thermal Conductance Calculation

Using the transmission function shown in Figure 3, the thermal conductance of the silicon clathrate nanowire with terminating hydrogens was calculated as a function of temperature, by numerically solving the conductance equation for temperatures ranging from 0 to 500 K, in increments of 20 K. The resulting graph is shown below in Figure 4, and the high temperature conductance limit of this system was determined to be approximately 0.475 nW/K. In comparison, a (7,0) carbon nanotube was determined to have a greater high temperature conductance limit of 4.50 nW/K [1].

### Acknowledgments

I would like to thank Dr. Mingo for his help in creating the phonon band diagram and collecting the transmission function data. I also appreciated the guidance of my mentor, Dr. Derek Stewart, and the financial contributions of the National Science Foundation, the National Nanotechnology Infrastructure Network Research Experience for Undergraduates Program, and the Cornell NanoScale Facility.

### References

- [1] N. Mingo, D.A. Stewart, D. A. Broido, and D.A. Shrivastava, "Phonon Transmission through Defects in Carbon Nanotubes from First-Principles", submitted to Phys. Rev. B.
- [2] B. Marsen and K. Sattler, Phys. Rev. B 60, 11593 (1999).
- [3] M. Durandurdu, Physica Status Solidi B, 243, R7-R9 (2006).
- [4] J. M. Soler et al., J. Phys. Condens. Matt., 14, 2745 (2002).
- [5] N Troullier and J.M. Martins, Phys. Rev. B 43, 1993.

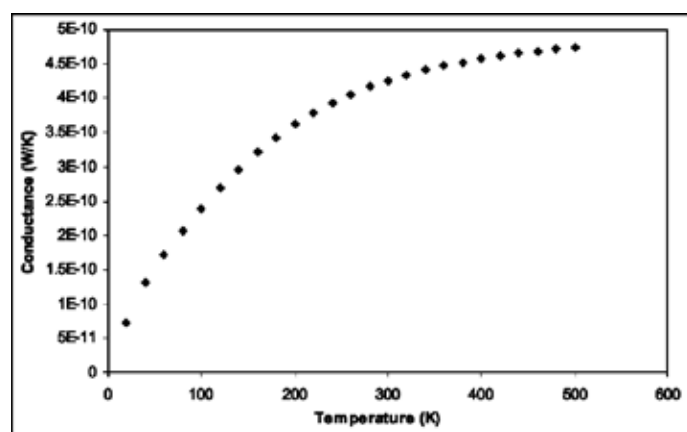


Figure 4: Thermal Conductance as a function of Temperature.